

Transient freezing of water in a square channel

An experimental investigation

Kaaks, Bouke Johannes; Lathouwers, Danny; Kloosterman, Jan Leen; Rohde, Martin

DOI

[10.1016/j.expthermflusci.2025.111417](https://doi.org/10.1016/j.expthermflusci.2025.111417)

Publication date

2025

Document Version

Final published version

Published in

Experimental Thermal and Fluid Science

Citation (APA)

Kaaks, B. J., Lathouwers, D., Kloosterman, J. L., & Rohde, M. (2025). Transient freezing of water in a square channel: An experimental investigation. *Experimental Thermal and Fluid Science*, 163, Article 111417. <https://doi.org/10.1016/j.expthermflusci.2025.111417>

Important note

To cite this publication, please use the final published version (if applicable). Please check the document version above.

Copyright


Other than for strictly personal use, it is not permitted to download, forward or distribute the text or part of it, without the consent of the author(s) and/or copyright holder(s), unless the work is under an open content license such as Creative Commons.

Takedown policy

Please contact us and provide details if you believe this document breaches copyrights. We will remove access to the work immediately and investigate your claim.



Transient freezing of water in a square channel: An experimental investigation

Bouke Johannes Kaaks, Danny Lathouwers, Jan-Leen Kloosterman, Martin Rohde *

Delft University of Technology, Department of Radiation Science and Technology, Mekelweg 15, Delft, 2629 JB, Netherlands

ARTICLE INFO

Dataset link: <https://doi.org/10.5281/zenodo.7573327>, <https://doi.org/10.5281/zenodo.7602394>

Keywords:

Transient freezing
Laminar internal flow
Particle image velocimetry
Experimental benchmark

ABSTRACT

This paper presents an experimental study for the transient growth of an ice layer in a square channel under laminar flow conditions and a mixed convection heat transfer regime. The ice layer was grown from a cold plate located at the bottom of the channel, capable of reaching temperatures between 0 and -20 °C. The onset of ice formation was marked by a sudden sharp increase of the cold plate temperature followed by a rapid spreading of the ice over the cold plate surface. This was attributed to subcooling effects within the thermal boundary layer of the flow. The flow field was measured using particle image velocimetry (PIV) and the ice profiles were measured at several instances of time after the onset of freezing by a visual tracing of the solid–liquid interface. In addition, a parametric study was performed regarding the effect of the cold plate temperature and the flow rate on the ice growth rate. Suitable approximations to the experimental boundary conditions were found after a detailed analysis of the cold plate's transient temperature response, which could be readily implemented in numerical software. An important novelty of the present work is the measurement of the transient ice development of the ice-layer near the inlet of the channel, in addition to the centre of the channel where the flow is more developed. As such, a comprehensive and well-described experimental data set was generated for transient freezing in laminar internal flow. With this approach, a very good agreement was obtained between the experimental results and numerical simulations which were included to indicate the suitability of the current experimental campaign for numerical benchmarking purposes.

1. Introduction

Melting and solidification phase change has been studied extensively in literature due to its complex physical and mathematical behaviour and its importance in applications such as metallurgy [1–3], latent heat storage [4,5] and GEN-IV nuclear reactors, in particular the Molten Salt Fast Reactor (MSFR). One of the main design features of the MSFR is the freeze-plug, which is a plug of solid salt located at the bottom of the reactor core that is designed to melt in case of a reactor anomaly [6].

For the design and safety of the MSFR, an accurate understanding of the melting and solidification phenomena is needed for a reliable calculation of the melting times of the freeze-plug [6], the prediction of the possible formation and growth of a solid crust of salt on the reactor walls during normal operation [7] and the analysis of accident scenarios where solidification poses a risk [8,9]. An example of such an accident scenario is the sudden solidification inside a heat exchanger. Therefore, there is a need to have a proper understanding of such conditions, and to improve the current numerical modelling capabilities

for transient freezing, specifically in internal flows where the wall temperature drops to below the melting point.

Many experimental studies have been performed on melting or freezing in an enclosure, characterized by a natural convection heat transfer regime. Examples are the melting of gallium in a rectangular enclosure with a heated side wall [1,3], the melting of octadecane in a rectangular enclosure with a heated side-wall [4,5] and the freezing of water in a cubical enclosure [10]. However, for freezing in internal flow, characterized by a forced or mixed convection heat transfer regime, the available quantitative experimental data is more limited, especially regarding the transient growth of the ice layer.

The earliest experimental investigations of freezing in internal flow provided data on the heat-transfer at the cooled wall as well as evidence of sub-cooling of the liquid phase [11–13]. Subsequent investigations focused on steady state freezing under a laminar flow regime [14–16], the effect of a transition from laminar to turbulent flow on the morphology of the ice layer [17–22] and the conditions under which a so-called freeze-off may occur [23].

* Corresponding author.

E-mail address: M.Rohde@tudelft.nl (M. Rohde).

Nomenclature**Acronymns**

AOI	Area Of Interest
CMOS	Complementary Metal Oxide Semiconductor
ESPRESSO	ExPERiment for RE-melting and Salt SOLidification
FOV	Field Of View
MSFR	Molten Salt Fast Reactor
PCM	Phase Change Material
PMMA	Poly(Methyl MethAcrylate)
PTU	Programmable Timing Unit

Dimensions

d	diameter (m)
D_h	hydraulic diameter (m)
H, W, L	height, width, length (m)
x, y, z	cartesian coordinate system (m)

Physical quantity

λ	wave length (nm)
ϕ	flow rate ($L s^{-1}$)
g	gravitational acceleration ($m s^{-2}$)
H	volumetric enthalpy ($J m^{-3}$)
m	mass flux ($kg m^{-2} s^{-1}$)
P	power (W)
p	pressure (Pa)
t	time (s, min or h)
T	temperature ($^{\circ}C$ or K)
u	velocity ($m s^{-1}$)

Thermophysical property

α	thermal diffusivity ($m^2 s^{-1}$)
β	thermal expansion coefficient (K^{-1})
μ	dynamic viscosity (Pa s)
ρ	density ($kg m^{-3}$)
c_p	specific heat ($J kg^{-1} K^{-1}$)
k	thermal conductivity ($W m^{-1} K$)
L	latent heat of fusion ($kJ kg^{-1}$)

Optics

δ_z	depth of view
f	focal length of the camera

$f^{\#}$	aperture of the camera
M_0	magnification factor
Z_0	image distance from the centre of the lens to the image plane
z_0	object distance to the effective centre of the lens

Lin. enthalpy model parameters

α	liquid fraction
ω	parameter to speed up the convergence
b	small parameter to prevent division by zero

C	Darcy constant
res	residual
tol	tolerance

Dimensionless numbers

$\theta_c = \frac{T_m - T_C}{T_H - T_m}$	cooling parameter
$Pe = Re Pr$	Péclet number
$Pr = \frac{\mu c_p}{k}$	Prandtl number
$Ra = \frac{g \beta \Delta T H^3}{\nu \alpha}$	Rayleigh number
$Re = \frac{\rho u D_h}{\mu}$	Reynolds number
$Ri = \frac{Ra}{Pr Re^2}$	Richardson number
$Stk = \frac{\rho_p d_p^2 u_{sc}}{18 \mu H}$	particle Stokes number

Other symbols

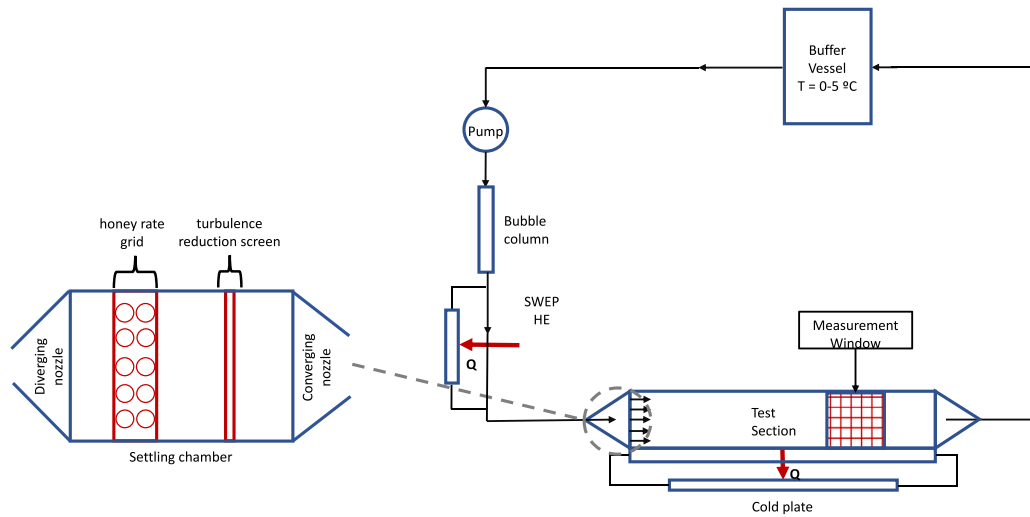
Δ	incremental difference
σ	uncertainty
N	Number of samples

Subscript

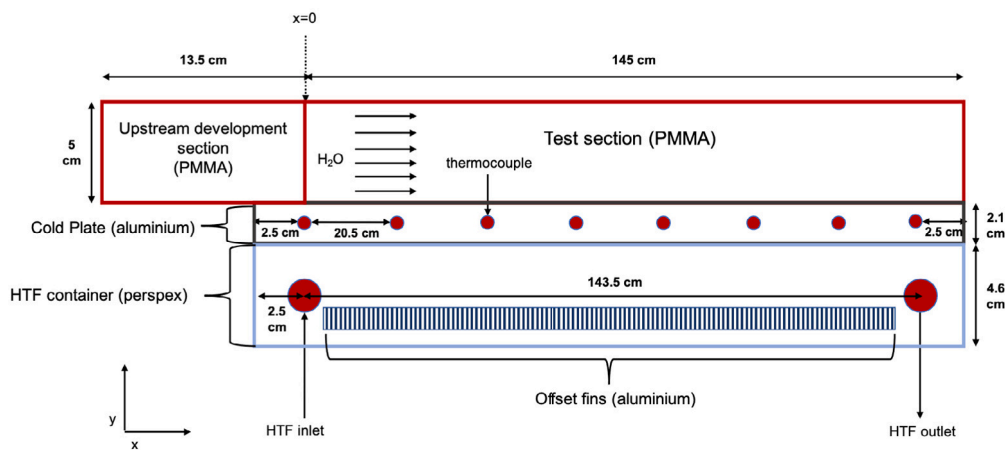
∞	bulk
c	of the cold plate
l	liquid
m	at the melting point
s	solid
$c_{,set}$	of the cold plate setpoint
in	of the inlet
$stat$	statistical
sys	systematic

Whereas the previous studies focused on the study of the steady state ice layer (or the question of whether a steady state ice layer may be formed under a given condition), transient freezing has mainly been studied theoretically using an analytical or numerical treatment (see for instance Ozisik et al. [24] or Weigand et al. [25]). This is believed to be due to the difficulty in accurately measuring the increase in the ice layer thickness [9]. Only four studies detailing the transient development of the ice layer in internal flow were found in literature. These are the freezing of water flowing over a chilled flat plate experiment by Savino et al. [26] performed in the 1960s and three recent studies including a study of the transient melting of an ice layer formed in a cylinder with a rotating lid after the onset of turbulent mixing [27], the study of the transient development of ice-scallops in a turbulent channel flow [28], and the study of the transient development of an ice layer in a laminar flow between two parallel plates under a constant heat flux condition [9].

In this work, we present experimental results of the transient freezing of water in a square channel with a cold-temperature plate at the bottom. The primary aim of this experimental campaign is to generate the most comprehensive experimental data set of freezing in laminar internal flow up to date, to be used for numerical benchmarking purposes. To this end, particle image velocimetry (PIV) measurements and ice profile measurements (using a manual extraction from photographic observations) were performed at different time-instances and for a variety of flow rates and cold plate temperatures. Special attention was paid to the selection of simple experimental boundary conditions, which can readily be implemented in numerical methods. Compared to the experiments of Savino et al. and Voulgaropoulos et al. [9,26] who only conducted transient ice growth measurements in the centre of the channel where the heat transfer is close to one-dimensional, and Hirata et al. and Kikuchi et al. [14,15] who conducted steady-state measurements of the ice-profiles near the inlet of the channel, the measurements of the transient ice growth near the inlet of the channel is an important novelty of the present experimental campaign. Finally, a comparison between the experimental data with numerical



(a) Sketch of ESPRESSO Experimental Facility.



(b) Zoom in of test section (side view).

Fig. 1. Graphical representation of ESPRESSO experimental facility. Here, PMMA stands for poly(methyl methacrylate), HE stands for heat exchanger and HTF stands for heat transfer fluid.

simulations is provided to illustrate the suitability of the performed experiments for numerical benchmarking purposes.

The remaining paper will cover the description of the experimental setup, the experimental procedure and the applied PIV and interface tracking methods (Section 2), the numerical method used for simulating the transient freezing of water in a square channel (Section 3) and the results of the experimental campaign including an analysis of the experimental boundary conditions and the comparison of experimental with numerical results (Section 4).

2. Experimental method

2.1. Design of ESPRESSO facility

Fig. 1 depicts a graphical representation of the ESPRESSO (ExPeriment for RE-melting and Salt Solidification) facility. ESPRESSO was designed with the objective of generating experimental data suitable for numerical benchmarking purposes for ice growth in internal flow where the wall temperature drops to below the melting point, a case of particular interest to the MSFR. As such, a special effort was made to impose well described and simple experimental boundary conditions that may readily be implemented in numerical software. For practical

reasons, in particular the high melting point of molten salt, water was used as the phase change material. Water was considered a suitable choice, because it is liquid at room temperature, its thermophysical properties are well-known and its *Prandtl* number is of a similar order of magnitude as that of the fuel salt [29,30]. In addition, experimental data on the freezing of water in internal flow has already been used for validating a thermal hydraulic code for simulating the freezing of molten salts in pipe flows in the MSFR [8]. However, water exhibits an anomalous expansion behaviour during the freezing process, with a density inversion around 4 °C. This may lead to phenomena such as penetrative Rayleigh-Bénard convection [31] or flow reversal during solidification [32]. Therefore, we recommend some caution when extrapolating the results from the current experimental campaign to the MSFR.

The ESPRESSO facility consists of a water tunnel with a square channel test-section ($H \times W \times L = 5.00 \pm 0.03 \text{ cm} \times 5.00 \pm 0.03 \text{ cm} \times 145.0 \pm 0.1 \text{ cm}$), made of poly(methyl methacrylate) (PMMA) in order to guarantee optical access. The side walls of the test section have a thickness of $d = 5.0 \pm 0.1 \text{ mm}$ and the removable top lid has a thickness of $d = 2.00 \pm 0.02 \text{ cm}$. The ice layer is grown from an aluminium cold plate at the bottom of the test section ($H = 2.10 \pm 0.02 \text{ cm}$, $L = 148.5 \pm 0.1 \text{ cm}$, $W = 9.50 \pm 0.03 \text{ cm}$) capable of reaching a minimum

temperature of $T_c = -20.0^\circ\text{C}$.

The cold plate is connected to an offset fin heat sink ($H = 4.60 \pm 0.03$ cm), containing 14 offset fins (1/8 lanced offset from Robinson Fin Machines, USA) with a flow length of $L = 15.00 \pm 0.03$ cm, a height of $H = 2.35 \pm 0.01$ cm and a thickness of $d = 0.025$ cm (geometrical tolerance unknown). The rest of the heat sink is made of PMMA, to provide thermal insulation. The use of offset fins offers better heat transfer capabilities as compared to the more conventional rectangular fin configuration [33]. The heat sink is coupled to a *Julabo FL1701* recirculating cooler, with a maximum power of $P = 1.7$ kW and a maximum flow rate of $\phi_v = 23.0$ L min⁻¹. The coolant used is *Julabo's Thermal G* (i.e. an ethylene-glycol water mixture). A series of 8 thermocouples with an accuracy of $\pm 0.2^\circ\text{C}$ are equally distributed along the length of the cold plate at a spacing of 20.5 cm. The thermocouple tips are inserted at a height of $H = 1.05 \pm 0.02$ cm and a depth of $W = 5.00 \pm 0.03$ cm, in the centre of the cold plate.

To impose a uniform inlet velocity profile at the entrance of the test section, the upstream section features a combination of a diffuser, settling chamber and a converging nozzle. Following the design heuristics of *Mehta et al.*, we selected a diffuser with an opening angle of 20° and 3 gauze screens installed [34]. The settling chamber has a cross-section of $H \times W = 15.00 \pm 0.05$ cm \times 15.00 ± 0.05 cm and a length of $L = 30.00 \pm 0.05$ cm, and contains a combination of a honey comb grid with an opening of 1.5 ± 0.1 mm to remove swirl and lateral turbulence and 3 screens (one coarse screen with an opening of 4.0 mm and two fine screens with an opening of 1.0 mm, geometrical tolerances unknown) for the reduction of axial turbulence [35]. The contraction shape of the nozzle is described by the following 5th order polynomial [36]:

$$y(x) = 0.5H_e + 0.5(H_i - H_e) \left[6 \left(\frac{x}{L} \right)^5 - 15 \left(\frac{x}{L} \right)^4 + 10 \left(\frac{x}{L} \right)^3 \right] \quad (1)$$

Here, H_i is the height of the nozzle at the nozzle inlet, H_e is the height of the nozzle at the nozzle exit, and L is the length of the nozzle. Due to geometric constraints, a development length of $L = 13.50$ cm long (more than 2 times the hydraulic diameter of the test section) was included between the outlet of the converging nozzle and the entrance of the test section.

The water is stored in a buffer vessel of approximately 100 L in volume and recirculated through the test section by a pump with an electronic frequency drive, capable of reaching a maximum flow rate of $\phi_v = 1.4$ L s⁻¹. To remove the (large) air bubbles introduced by the pump, the flow is passed through a bubble column. A brazed plate liquid heat exchanger (SWEP, Sweden), located after the pump and coupled to a second *Julabo FL1701* recirculating cooler,¹ is used for controlling the inlet temperature between a range of approximately 20 and 5 °C. In addition to the temperatures of the cold plate, the temperatures of the buffer vessel as well as the bulk inlet and outlet temperatures are recorded using K-type thermocouples. The flowrate is recorded using a Proline Promag 10 W magnetic flow metre (Endress Hauser, Germany) with an accuracy of $\sigma_{\phi_v} = \pm 0.5\%$ or $\sigma_u = \pm 2$ mm s⁻¹ for flow-rates outside the official measurement range. Finally, to limit the heat flux through the side walls and the top lid, the test section is thermally insulated using styrofoam, except in those regions where optical access is needed.

2.2. Particle image velocimetry

We measured the velocity in a two-dimensional xy -plane using a planar particle image velocimetry (PIV) measurement technique. The flow was seeded with hollow borosilicate glass spheres (LaVision, Germany), with an average density of $\rho = 1.1$ g cm⁻³ and a mean diameter of $d_p = 10$ μm. For a bulk velocity of $u_\infty \approx 1.5$ cm s⁻¹, the particle Stokes

number is defined as

$$Stk = \frac{\rho_p d_p^2 u_\infty}{18\mu D_h} \approx 1.5 \cdot 10^{-6}. \quad (2)$$

Therefore, the velocity lag of the particles was considered to be negligible [37]. A class-IV, 5 W shuttered continuous wave laser (diode pumped, solid-state) with a wave length of $\lambda = 532$ nm (LaVision, Germany) was used as the light source of the PIV images. The laser sheet was generated through a combination of a spherical and a cylindrical lens, with a beam waist thickness of approximately 1 mm. A laser guiding arm (LaVision, Germany) was used to introduce the laser sheet from the top of the test section. The motion of the particles and the growth of the ice layer was imaged from the side using a Complementary Metal-Oxide Semiconductor (CMOS) Imager MX-4M (LaVision, Germany) camera with 4 MP of resolution (pixel size of $5.5 \mu\text{m} \times 5.5 \mu\text{m}$) and mounting an AF-S 50 mm F/1.4 (Nikon) lens. To ensure maximum overlap between the field of view (FOV) and the area of interest (AOI), the camera was located at approximately 40 cm from the centre of the channel and in-focus images were obtained using a focus close to the maximal focal length of 50 mm. Subsequently, the magnification factor is defined as

$$M_0 = \frac{Z_0}{z_0}, \quad (3)$$

where Z_0 is the image distance from the centre of the lens to the image plane and z_0 is the object distance to the effective centre of the lens (i.e. 40 cm). Z_0 is estimated applying the *Gauss* lens law

$$\frac{1}{Z_0} + \frac{1}{z_0} = \frac{1}{f}, \quad (4)$$

where f is the focal length of the camera, resulting in a magnification factor of approximately $M_0 = 0.14$. To obtain sufficient exposure, we selected a laser pulse duration of $t = 1000$ μs and an aperture of $f^\# = 4.0 - 5.6$. This yields the following depth of field [37]:

$$\delta_z = 4 \left(1 + \frac{1}{M_0} \right)^2 f^\#^2 \lambda = 2.0 - 4.4 \text{ mm}, \quad (5)$$

where δ_z is the depth of view and λ is the wavelength of the laser. Since the depth of view is larger than the beam waist thickness of the laser, all PIV particles within the laser sheet are considered to be in focus. A single-pulsed, double-frame recording mode was used, with a pulse separation of $dt = 10$ ms and $dt = 5$ ms for $Re = 474$ and $Re = 1118$ respectively based on a desired mean particle displacement shift of approximately 5 pixels. At each measurement, 25 pairs of images were recorded with a frequency of 10 Hz. The camera and laser were synchronized using a programmable timing unit (PTU, LaVision, Germany), operated by the Davis v8 software.

2.3. Experimental procedure

The velocity fields and ice layer profiles were measured for two different flow rates (corresponding to $Re = 474$ and $Re = 1118$) and four different set point temperatures of the cold plate (i.e. $T_{c,set} = -5^\circ\text{C}$, $T_{c,set} = -7.5^\circ\text{C}$, $T_{c,set} = -10^\circ\text{C}$ and $T_{c,set} = -15^\circ\text{C}$). Measurements were performed at both the inlet (thermal entrance region) and at the centre of the test section where the heat transfer is close to one-dimensional. The experiment was initialized as follows. First the water was recirculated at the maximum available flow rate whilst the cold plate and the inlet were cooled to the desired temperatures. After the cold plate reached a temperature of around $T_c = -1.5^\circ\text{C}$, the flow rate was reduced to the desired value. Sometimes, the sudden lowering of the flow-rate resulted in the release of air bubbles, obstructing the laser sheet.² To remove these air bubbles from the test section, the flow rate was increased again to 100% capacity and multiple iterations of increasing and decreasing the maximum flow-rate could be needed

¹ Instead of ethylene glycol, the second recirculating cooler uses water as the coolant.

² Especially smaller air bubbles may pass through the bubble column.

until the lowering of the flow-rate no longer resulted in the release of air bubbles. Subsequently, the flow rate remained fixed at the desired set point value.

Because the cold plate was in direct contact with the water flow above, reducing the flow rate of the water (and therefore the heat exchange between the water and the surface of the cold plate) resulted in a further decrease of the cold plate temperature. As soon as the cold plate reached a temperature below $T_c = -2.0^\circ\text{C}$, freezing would occur, consistent with the findings of *Voulgaropoulos et al.* [9]). The onset of freezing was marked by a sudden sharp increase of the measured cold plate temperature, which was therefore used to determine $t = 0$ in our experiments (see Section 4.3).

Whilst this approach to initialize the experiment resulted in a significant transient in the cold plate, it was highly reproducible. Alternatively, an initialization approach was considered where the cold plate was cooled until the set point temperature was reached, upon which the test section was filled with water. However, this approach was more difficult to reproduce whilst resulting in a similarly large temperature transient in the cold plate after filling the test section. During the first hour after the onset of ice-formation at $t = 0$, an image recording was made every 5 min. During the second hour, this frequency was reduced to each 15 min and after the third hour to 30 min. Preliminary tests showed this temporal resolution was sufficient to capture the transient growth of the ice layer. During the experiments, the temperatures measured by the thermocouples as well as the flow rate were recorded in real time and stored using the LabView software.

2.4. Image analysis and estimation of errors

2.4.1. Ice layer thickness measurements

The camera images were visually and manually translated from the image plane to the physical space using the height of the channel as a reference distance, followed by a rotation correction to correct for a slight tilting of the camera lens of approximately $0.5 - 0.6^\circ$ using the edge of the cold plate as a reference line. Because light diffraction was very small thanks to the planar surface of the test section, and image distortion effects due to the curvature of the lens were considered to be negligible [37], this image calibration was sufficient in our case. Sufficient contrast between the ice and the water allowed for a manual evaluation of the ice-water interface position using the *WebPlotDigitizer* software (similar to the approach used by *Faden et al.* [5]).

The following sources of uncertainty were identified in the measurements of the ice layer profiles:

1. An estimated uncertainty of approximately 0.5% in the x and approximately 0.25% y scale calibration. The estimated uncertainty in the x scale calibration is larger due to a higher difficulty in identifying $x = 0$ as compared to $y = 0$.
2. An uncertainty in identifying the zero time instant (time at which the onset of ice-formation first occurred), estimated at ± 3 s. This uncertainty is very small compared to the duration of the transient ice-growth experiments, which was two hours.
3. An uncertainty in timing the subsequent image samples. This uncertainty was estimated at ± 5 s for the 5 min intervals and ± 15 s for the 15 min and 30 min intervals.
4. An uncertainty in the exact manual tracing of the solid-liquid interface. The exact size of this uncertainty was difficult to determine, however based on our personal experience it was estimated to be around ± 0.05 mm. This uncertainty was larger close to the inlet of the channel, where low laser light intensity combined with the formation of condense could lead to poor image quality.

It is difficult to gauge the combined effect of the individual uncertainties. For this reason, a series of 5 independent measurements was performed for the same experimental conditions, i.e. $Re = 474$ and $T_{c,set} = -10^\circ\text{C}$. From the post-processed ice layers, an uncertainty of

approximately 0.1–0.2 mm was obtained, which is between 0.2–0.4% of the channel height. As such, these experiments were considered to be sufficiently reproducible and reliable.

2.4.2. Velocity measurements

The images were pre-processed to enhance the signal to noise ratio of the particles. The pre-processing step consisted of the application of a non-linear sliding average filter, applied over 5 pixels and subtracted from the images, followed by a min-max filter and an intensity normalization filter. Due to the transient nature of the experiments (i.e. the growth of the ice layer) and its effect on the laser scattering signal, no background subtraction was performed. The velocity vectors were calculated using a multi-pass option where the initial size of the correlation window was 64×64 pixels and after three passes the window size was decreased towards 32×32 for the final pass. The postprocessing consisted of a median filter to remove outliers as well as the removal of out of bounds velocity values, followed by a statistical averaging and a 3×3 Gaussian smoothing filter.

The following sources of uncertainty were considered:

1. A statistical uncertainty σ_{stat} given by:

$$\sigma_{stat} = \frac{\sigma}{\sqrt{N}} = \sqrt{\frac{1}{N_t N_x N_y (N_t - 1)} \sum_{i=1}^N (u_i - \bar{u})^2}, \quad (6)$$

where σ is the standard deviation, $N = N_t N_x N_y$ is the total number of samples, N_t is the number of time samples (25 in our case), N_x and N_y are the number of pixels in the x - and y -direction over which smoothing is applied (3,3 respectively) and \bar{u} is the mean value of the velocity.

2. A systematic uncertainty (σ_{sys}), resulting from the uncertainties in the x and y scale calibration (see Section 2.4.1). The systematic uncertainty is evaluated by:

$$\sigma_{sys} = \sqrt{\left(\frac{\partial u_x}{\partial x} \Delta x\right)^2 + \left(\frac{\partial u_x}{\partial y} \Delta y\right)^2 + \left(\frac{\partial u_y}{\partial x} \Delta x\right)^2 + \left(\frac{\partial u_y}{\partial y} \Delta y\right)^2}, \quad (7)$$

where Δx and Δy are the tolerances in the calibration of the x and y scales respectively. Possible other systematic uncertainties were considered ‘unknown unknowns’, and were therefore not included.

Assuming independence of the statistical and systematic errors, the total uncertainty in the velocity measurements was estimated as:

$$\sigma_{tot} = \sqrt{\sigma_{stat}^2 + \sigma_{sys}^2} \quad (8)$$

The statistical variation of the velocity (σ_{stat}) was used to confirm laminarity of the flow. The standard deviation was approximately 2% of the bulk velocity value (which gives an uncertainty of approximately 0.04% due to the number of time samples and the applied smoothing), and spatial coherence was absent apart from the regions where a larger uncertainty could be expected due to poor optical access or reflections (such as close to the ice layer). These results for the statistical uncertainty were consistent with our expectations for laminar flow.

3. Numerical methodology

3.1. Governing equations

The numerical modelling of melting and/or solidification is challenging, due to the non-linear displacement of the interface in time and the discontinuity in the enthalpy and the temperature gradient of the phase change material across the interface (see Fig. 2).

Assuming constant thermophysical properties in each phase, and neglecting volume expansion as a consequence of the difference in densities between the solid and liquid phases, the enthalpy-temperature

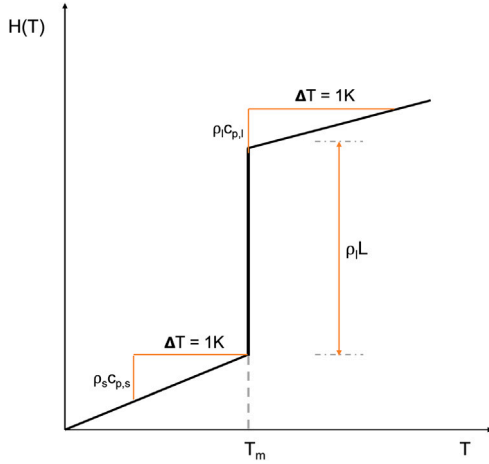


Fig. 2. Enthalpy-temperature relationship for isothermal solid-liquid phase change.

relationship can be written as a piece-wise continuous function

$$T(H) = \begin{cases} \frac{H}{\rho_s c_{p,s}}, & H \leq \rho_s c_{p,s} T_m \\ T_m, & \rho_s c_{p,s} T_m < H < \rho_s c_{p,s} T_m + \rho_l L \\ T_m + \frac{H - (\rho_s c_{p,s} T_m + \rho_l L)}{\rho_l c_{p,l}}, & H \geq \rho_s c_{p,s} T_m + \rho_l L, \end{cases} \quad (9)$$

where ρ is the density in kg m^{-3} , c_p is the specific heat capacity in $\text{J kg}^{-1} \text{K}^{-1}$, L is the latent heat in J kg^{-1} , T_m is the melting temperature and the subscripts 's' and 'l' indicate the solid and liquid phases respectively.

Roughly speaking, the various numerical approaches for modelling melting/solidification problems may be divided along the lines of 'single domain' versus 'multi domain' and 'explicit' versus 'implicit' interface representation. In the single domain class of methods with an implicit interface representation, the solid and liquid phases are represented by a single mesh and the interface position is obtained from the local energy solution, instead of being obtained from the solution of a separate equation. This class of methods has the advantage of not requiring the use of mesh generation and not depending on complex thermodynamical derivation or the calculation of interface curvatures.

The present work employs a mixed-order discontinuous Galerkin method based on the 'linearized enthalpy approach' [38]. Contrary to the source-based enthalpy approach [39] and the apparent heat capacity method [40], the linearized enthalpy approach is based on the conservative form of the energy transport equation (and is therefore inherently thermal energy conservative) and does not rely on the use of a so-called mushy zone. The Darcy source-term is used for enforcing the no-slip condition at the solid-liquid interface. The set of coupled energy, momentum and continuity equations therefore reads:

$$\frac{\partial H}{\partial t} + \rho_l c_{p,l} \nabla \cdot (\mathbf{u}T) = \nabla \cdot (k \nabla T). \quad (10)$$

$$\frac{\partial (\rho_l \mathbf{u})}{\partial t} + \nabla \cdot (\mathbf{u} \otimes (\rho_l \mathbf{u})) = \nabla \cdot [\mu (\nabla \mathbf{u} + (\nabla \mathbf{u})^T)] - \nabla p + \rho_l g \beta (T - T_m) - C \frac{(1 - \alpha)^2}{\alpha^3 + b} \mathbf{u}. \quad (11)$$

$$\nabla \cdot \mathbf{u} = 0. \quad (12)$$

3.2. Discretization and solution procedure

The above system of equations is discretized using the discontinuous Galerkin method, which combines attractive features of the finite

element and finite volume methods, i.e., an arbitrarily high order of accuracy, geometric flexibility, local conservation, possibility for up-winding and a compact stencil facilitating efficient parallelization [41, 42]. A brief overview of the applied numerical method is given here, for further detail please refer to the original paper [38].

The semi-discrete variational formulation of the above system of equations reads

Find $m_h \in \mathcal{V}_{h,m}^d$ and $p_h \in \mathcal{V}_{h,p,H,T}$ and $H_h \in \mathcal{V}_{h,p,H,T}$ and

$T_h \in \mathcal{V}_{h,p,H,T}$ such that, $\forall v_h \in \mathcal{V}_{h,m}^d$ and $\forall q_h, \forall w_h \in \mathcal{V}_{h,p,T,H}$,

$$\sum_{\mathcal{T} \in \mathcal{T}_h} \int_{\mathcal{T}} \mathbf{v}_h \cdot \frac{\partial m_h}{\partial t} + a^{\text{conv}}(\mathbf{u}_h, m_h, \mathbf{v}_h) + a^{\text{diff}}(m_h, \mathbf{v}_h) + a^{\text{div}}(\mathbf{v}_h, p_h) \quad (13a)$$

$$+ a^{\text{source}}(m_h, \mathbf{v}_h) = l^{\text{conv}}(\mathbf{u}_h, \mathbf{v}_h) + l^{\text{diff}}(\mathbf{v}_h) + l^{\text{source}}(\mathbf{v}_h, T_h)$$

$$a^{\text{div}}(m_h, q_h) = l^{\text{div}}(q_h) \quad (13b)$$

$$\sum_{\mathcal{T} \in \mathcal{T}_h} \int_{\mathcal{T}} w_h \frac{\partial H_h}{\partial t} + a^{\text{conv}}(m_h, T_h, w_h) + a^{\text{diff}}(T_h, w_h) \quad (13c)$$

$$= l^{\text{conv}}(\mathbf{u}_h, w_h) + l^{\text{diff}}(w_h)$$

$$T_h = T(H_h). \quad (13d)$$

The temperature, enthalpy, mass-flux and pressure solutions on each local element T_h are approximated using a hierarchical set of orthogonal modal basis functions (normalized Legendre polynomials). A mixed order formulation is used, that is $P_{p,H,T} = P_m - 1$. Contrary to an equal order formulation, the mixed order formulation does not rely on pressure stabilization terms. The diffusive term is discretized using the symmetric interior penalty method and the Lax-Friedrichs flux is used for the convective term.

The semi-discrete energy equation effectively contains two unknowns, i.e. the enthalpy and the temperature, coupled together through the non-linear enthalpy-temperature relationship. As such, the semi-discrete energy equation cannot be solved directly and is instead linearized by expanding the unknown enthalpy at the latest time-step around the newest temperature value:

$$H_h^{n+1,i+1} = H_h^{n+1,i} + \frac{dH}{dT} \Big|_{n+1,i} (T^{n+1,i+1/2} - T^{n+1,i}), \quad (14)$$

where the superscript $i + 1$ refers to the new iteration, and $i + 1/2$ refers to an intermediate value between two iterations. Inserting the expansion into the discretized energy equation yields the 'linearized' discretized energy equation:

$$\sum_{\mathcal{T} \in \mathcal{T}_h} \int_{\mathcal{T}} w_h \frac{3H_h^{n+1,i} - 4H_h^n + H_h^{n-1}}{2\Delta t} + \sum_{\mathcal{T} \in \mathcal{T}_h} \int_{\mathcal{T}} \frac{dH}{dT} \Big|_{n+1,i} w_h \frac{3T_h^{n+1,i+1/2} - 3T_h^{n+1,i}}{2\Delta t} + a^{\text{conv}}(m_h, T_h^{n+1,i+1/2}, w_h) + a^{\text{diff}}(T_h^{n+1,i+1/2}, w_h) = l^{\text{conv}}(\mathbf{u}_h, w_h) + l^{\text{diff}}(w_h). \quad (15)$$

Here, the enthalpy-temperature derivative is approximated as follows:

$$\frac{dH}{dT} \approx \begin{cases} \omega \rho_s c_{p,s}, & T \leq T_m \\ \omega \rho_l c_{p,l}, & T > T_m, \end{cases} \quad (16)$$

where $\omega = 1.5$ is a parameter to speed up the convergence. It has been shown previously that replacing the true enthalpy-temperature derivative with an approximation still yields the same accuracy of results [43], and $\omega = 1.5$ was found to be the best compromise between a faster convergence of the energy equation and stability [38]. The iterative solution procedure is described by the following steps:

1. Initialize the enthalpy at the new time-step $H^{n+1,i}$ through an extrapolation from previous time-steps.
2. Solve the discretized linearized energy transport equation to obtain the solution for the intermediate temperature.

3. Update the volumetric enthalpy at the quadrature points applying the Taylor linearization (see Eq. (14)).
4. At the quadrature points, calculate the temperature from the updated enthalpy values through the enthalpy-temperature relationship.
5. Calculate the solution coefficients of the enthalpy and temperature at the latest iteration, by projecting the values at the quadrature points onto the finite element basis for each element.
6. Check whether the convergence criterion:

$$\max \left(\frac{res}{E_{tot}}, \left(\frac{\int_{\Omega} \left([T_h^{n+1,i+1} - T_h^{n+1,i}]^2 \right)^{1/2}}{\int_{\Omega} \left([T_h^{n+1,i+1}]^2 \right)^{1/2}} \right) \right) < tol \quad (17)$$

is satisfied. Here, the residual is a measure of how far the solution is from satisfying energy conservation (see [38] for more details. If not, return to step 2. If yes, move to the solution of the momentum equation.

The coupled energy and momentum equations are solved in a segregated manner, using a total of three outer iterations. To model the conjugate heat transfer, the energy equations for the solid metal domain and the 'liquid' PCM domain are solved simultaneously with no explicit interface condition being imposed. The momentum equation is solved only within the 'liquid' PCM domain, with the no-slip boundary condition being imposed on the solid-liquid interface.

3.3. Material properties and flow and heat transfer regime

The thermophysical properties of the water, ice and aluminium as used in the numerical simulations are given in Table 1. Constant thermophysical properties were considered for each phase, except for the thermal expansion coefficient which was calculated by the following temperature-dependent function to account for the anomalous expansion of water [29]:

$$\beta(T) = -6.88 \cdot 10^{-5} + 2.17 \cdot 10^{-5}T - 2.12 \cdot 10^{-6}T^{1.5} + 7.72 \cdot 10^{-8}T^2, \quad (18)$$

where T is the temperature in °C. Furthermore, the same density of 1000 kg m^{-3} was used for the ice and water phases. This was done to avoid the numerical complexity regarding the expansion of the water upon freezing [44].

Based on the thermophysical properties, and the inflow conditions, the flow and heat transfer regime was characterized as follows (depending on the imposed flow rate): $Re = \frac{\rho u_{\infty} H}{\mu} \approx 474$ or 1118 , $Pr = \frac{\nu}{\alpha} \approx 11$, $Pe = RePr \approx 5263$ or 12414 , $Ra = \frac{g\beta\Delta T H^3}{\nu\alpha} \approx -2.0 \cdot 10^6$, $Gr = Ra/Pr \approx 1.8 \cdot 10^5$ and $Ri = Gr/Re^2 \approx -0.8$ or -0.15 . Here, we considered a temperature difference of $\Delta T = 5 \text{ K}$ and a thermal expansion coefficient of $\beta(T) = -6.88 \cdot 10^{-5} \text{ K}^{-1}$ (evaluated at the melting point). As such, the flow is laminar with a mixed convection heat transfer regime. Therefore, we recommend to include the role of natural convection when using these experiments for numerical validation, especially for $Re = 474$.

The effect of natural convection is expected to decrease as the ice layer thickens, since the hydraulic diameter is reduced whilst the temperature difference between the ice and the bulk fluid remains constant. The Rayleigh number is above the critical value for which penetrative Rayleigh-Bénard phenomena have been observed [31]. However, Large et al. conducted their experiments for a fluid at rest, whilst in our case the fluid was in constant motion, which could prevent the onset of instabilities within the thermal boundary layer.

Table 1

Thermophysical properties of water and aluminium 7075-T6 as used in the numerical simulation.

	Water	Ice	Aluminium
Density [kg m^{-3}]	1000	1000	2810
Specific heat capacity [J kg^{-1}]	4200	2100	714.8
Thermal conductivity [$\text{W m}^{-1} \text{K}^{-1}$]	0.575	2.16	140.0
Latent heat [kJ kg^{-1}]	333		
Melting Temperature [K]	273		
Thermal expansion coefficient [$1/\text{K}$]	$f(T)$	N/A	
Dynamic viscosity [Pa s]	$1.52 \cdot 10^{-3}$		

3.4. Case setup

Fig. 3 shows a sketch of the two-dimensional computational domain, including the dimensions and the prescribed boundary condition. The transient temperature response measured by the thermocouples located in the centre of the cold plate, $T = T_c(t)$ (see Section 2.1, 4.3) was imposed as boundary condition at the bottom and the rest of the cold plate was simulated through a conjugate heat transfer simulation with the water flowing through the test section above. To avoid a conflict between the imposed uniform inflow condition and zero gradient outflow conditions and the presence of an ice layer, the test section was extended by 10cm in both directions. Apart from the bottom of the cold plate and the inflow boundary, the other boundaries were assumed to be adiabatic and the front and back were modelled with a symmetry boundary condition, due to the 2D nature of the simulation. We simulated the case corresponding to $Re = 474$, $T_{in} \approx 4.7 \text{ °C}$ and $T_{c,set} = -10 \text{ °C}$. An inflow velocity of $\vec{u}_{in,x} = 1.44 \text{ cm s}^{-1}$, $\vec{u}_{in,y} = 0 \text{ cm s}^{-1}$ was set and the following fits were used for the transient behaviour of the cold plate and the inlet temperature (see Section 4.3 for more detail regarding the choice of the boundary conditions):

$$T_c = 273 - 8.202 + 6.826 \exp\left(-6.404 \frac{t}{3600}\right) - 0.775 \tanh\left(0.431 \frac{t}{3600}\right) \quad (19)$$

$$T_{in} = 273 + 4.671 - 0.046 \exp\left(-1.346 \frac{t}{3600}\right), \quad (20)$$

where $t = 0$ is the onset of ice formation in the experiment.

The base mesh consists of 84,500 elements with a resolution of $\Delta x \cdot \Delta y = 0.25 \text{ cm} \cdot 0.05 \text{ cm}$ in the test section and a resolution of $\Delta x \cdot \Delta y = 0.25 \text{ cm} \cdot 0.035 \text{ cm}$ in the cold plate. In addition, two areas of interest were selected for performing local mesh refinement. Near the inlet the mesh was refined three times (so the resolution became 8 times finer), and in the centre of the channel the mesh was refined two times. The refined mesh consists of approximately 380,000 elements. Finally, a grading was applied in the streamwise direction: towards the inlet, the length of each element decreased according to $\Delta x_{elem} = \frac{1}{1.033} \Delta x_{elem-1}$ and away from the inlet the length of each element increased according to $\Delta x_{elem} = \frac{1}{1.002} \Delta x_{elem-1}$. A time-step of $\Delta t = 0.1 \text{ s}$ was used throughout the simulation.

The purpose of the numerical campaign was to demonstrate the suitability of the experimental results for numerical benchmarking purposes, using the boundary conditions which were derived from the experimental data. In order to reduce the complexity of the numerical model and to keep the simulations computationally affordable, the following simplifications were made:

1. Approximation of the experimental domain by a two-dimensional numerical domain, hereby neglecting the wall effect in the third dimension. This was done to keep the simulations computationally affordable.
2. The use of constant and isotropic thermophysical properties in each phase (see Table 1), except for a temperature dependent thermal expansion coefficient (see Eq. (18)) which was used together with the Boussinesq approximation to model mixed convection effects within the channel. A similar approach was

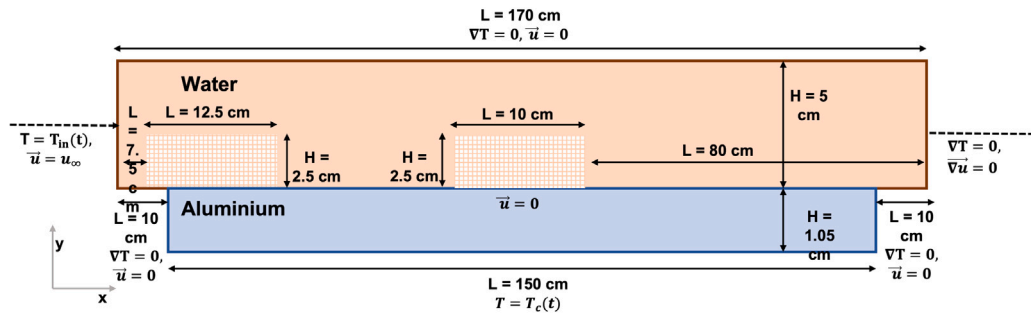


Fig. 3. Sketch of computational domain for simulating ice growth in a forced convection channel flow. The red and blue colours are used to distinguish the two different materials (i.e. water and aluminium). The square rosters in the water domain represent the two areas where mesh refinement was applied, i.e. at the inlet (8 times refined) and the centre of the test section (4 times refined).

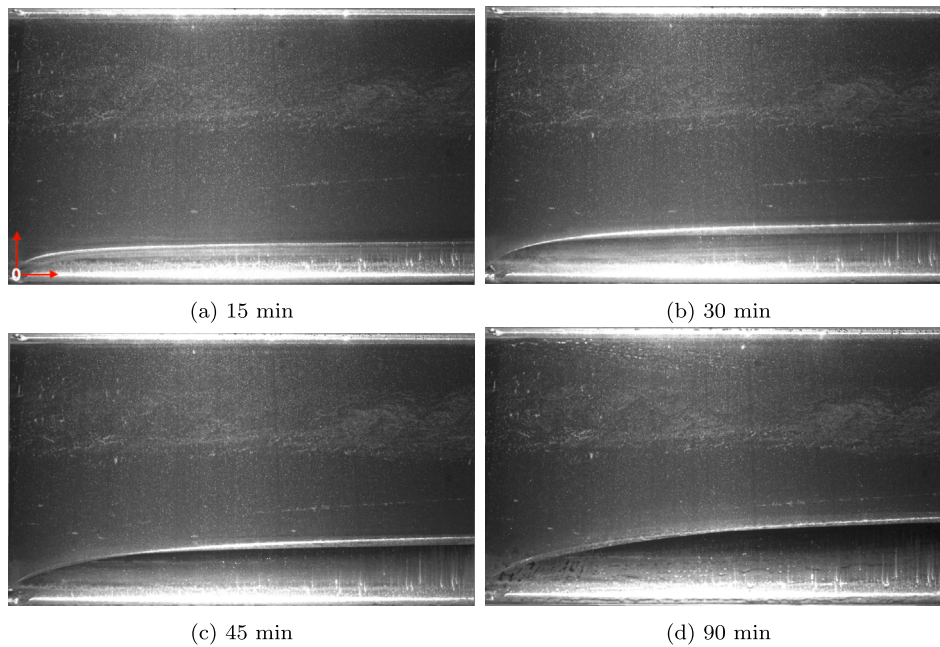


Fig. 4. Camera images of transient ice growth taken with the LaVision Imager MX4M close to the inlet of the test section, after respectively 15, 30, 45 and 90 min starting from the onset of ice formation. The experimental conditions were: $Re = 474$, $T_{in} \approx 4.7^\circ\text{C}$, $T_{c,set} = -10^\circ\text{C}$. The origin of the xy Cartesian coordinate system is indicated in the top left image.

used by *Belhamadia et al.* [45] to simulate the freezing of water in a cubic cavity, who obtained a very good agreement with the experimental reference data [10].

3. The use of an equal density for the solid and liquid phases. This is done to avoid the numerical complexity regarding the expansion of the water upon freezing [44].
4. Assumption of incompressible flow.
5. Use of the ‘sensible enthalpy’ only formulation for the convection of heat [46].

4. Results and discussion

4.1. Transient ice growth and velocity measurements

Fig. 4 depicts the camera images taken with the LaVision Imager MX4M of the first 8 cm of the ESPRESSO facility after respectively 10, 30 and 90 min of ice growth. The flow conditions were $Re = 474$, $T_{in} \approx 4.7^\circ\text{C}$ and $T_{c,set} = -10^\circ\text{C}$. Sufficient contrast between the ice layer and the water above allowed for a manual tracing of the solid–liquid interface position. The solid–liquid interface position was found to coincide with the scattering signal of the laser, also shown by *Voulgourapoulos et al.* [9]). The bottom and top wall boundaries, as

well as the solid–liquid interface, can be clearly distinguished due to their higher intensity value. The ice grows fastest near the inlet of the channel, with the ice layer profile becoming more and more flat as the downstream distance increases, consistent with the findings of *Zerkle et al.* and *Hirata et al.* [11,14].

The corresponding contour plots of the velocity in the xy -plane are given in Fig. 5, where the ice layer is characterized by very low velocities. The velocity vectors are included to indicate the direction of the flow. With the growth of the ice layer, the effective cross section decreases and consequently the flow accelerates (since a fixed flow-rate is imposed by the pump). We expect the pressure drop to increase correspondingly, based on the results provided by *Zerkle et al.* and *Mulligan et al.* [11,13]. Whilst the freezing of water from the bottom could potentially lead to penetrative Rayleigh–Bénard convection [31], no convection cells were present in the PIV results. Possibly, the constant motion of fluid prevents the development of Rayleigh–Bénard type instabilities. Finally, the expansion of the ice, as well as the onset of natural convection, could lead to the generation of secondary flow in the z -direction [47]. Therefore, we recommend the measurement of the spanwise (z) velocity components (for instance using stereoscopic PIV) as a subject for further investigation.

Fig. 6 shows the ice profiles after respectively 15, 30, 45 and 90 min of ice growth, obtained by carefully tracing the solid–liquid interface

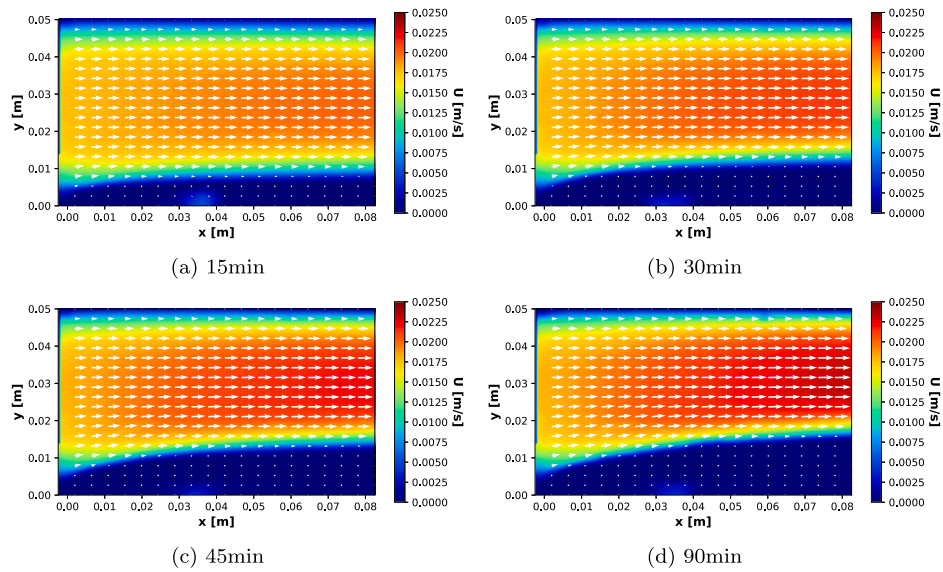


Fig. 5. Measured velocity fields after respectively 15, 30, 45 and 90 min starting from the onset of ice formation. The experimental conditions were: $Re = 474$, $T_{in} \approx 4.7\text{ }^\circ\text{C}$, $T_{c,set} = -10\text{ }^\circ\text{C}$.

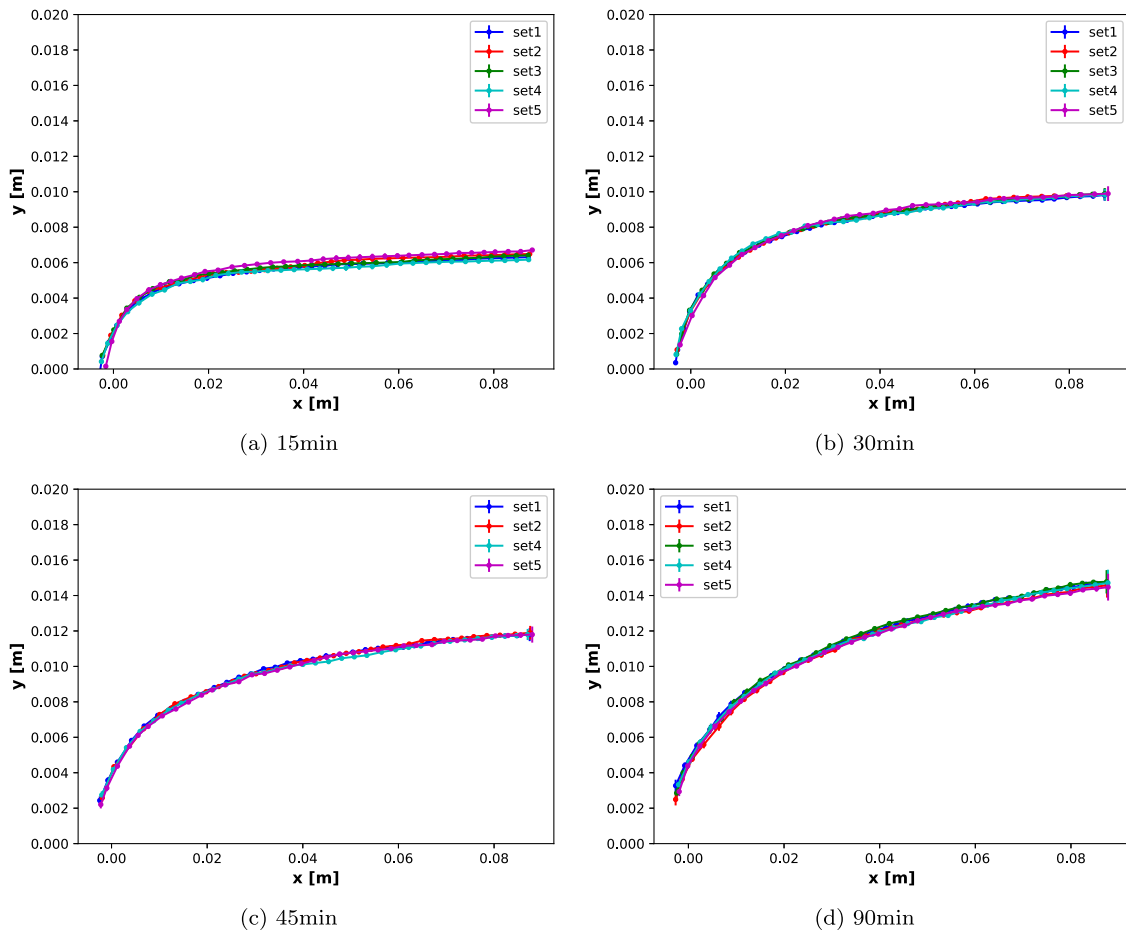


Fig. 6. Measured ice layer profiles after respectively 15, 30, 45 and 90 min starting from the onset of ice formation. 5 sets of independent measurements are given. The experimental conditions were: $Re = 474$, $T_{in} \approx 4.7\text{ }^\circ\text{C}$, $T_{c,set} = -10\text{ }^\circ\text{C}$. From these 5 measurements, an uncertainty of approximately $\sigma = 0.1\text{--}0.2\text{ mm}$ was calculated, as shown by the error bars.

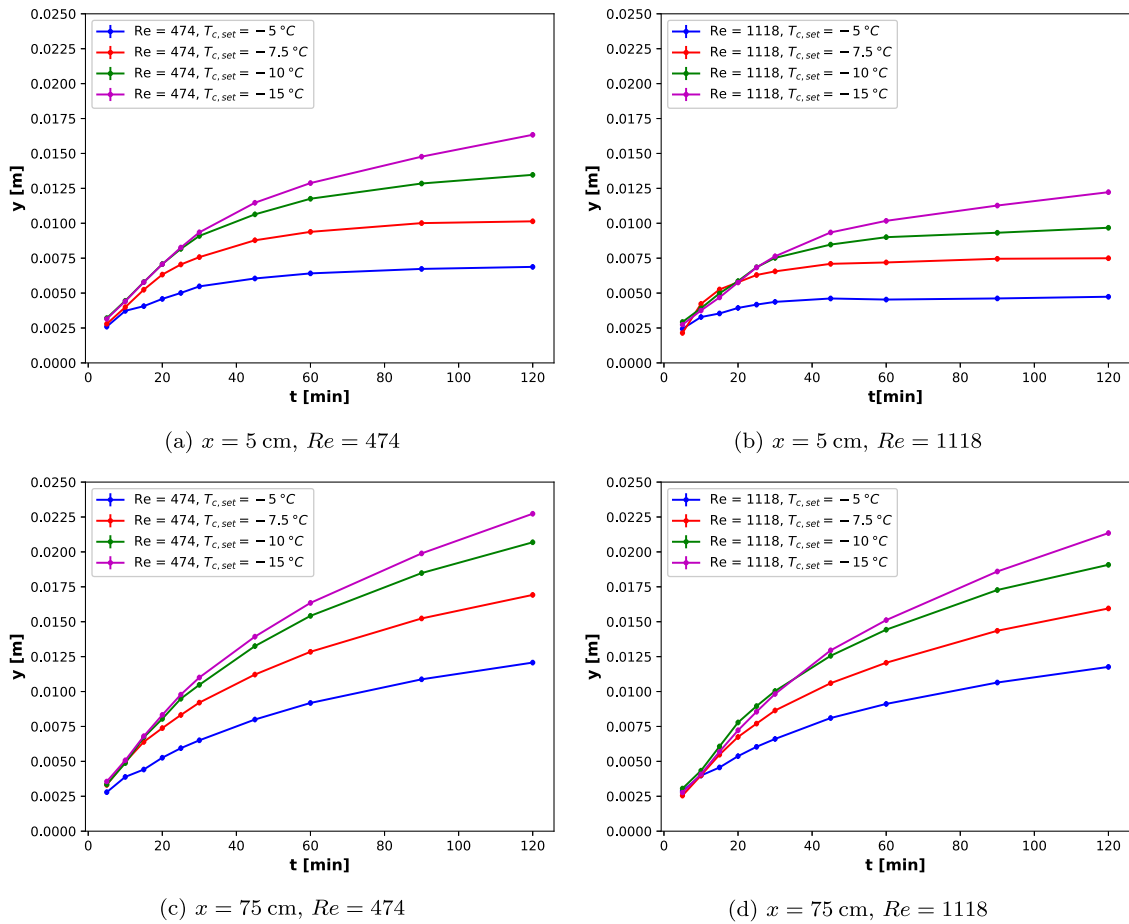


Fig. 7. Transient ice layer thicknesses for four different cold plate temperature set points and two different flow rates, evaluated close to the inlet of the channel at $x = 5$ cm and at the centre of the channel at $x = 75$ cm. From the set of five repeated measurements, the uncertainty in the ice layer is estimated at $\sigma = 0.1 - 0.2$ mm. Error bars are plotted for the conservative value of $\sigma = 0.2$ mm.

in the camera images (see Fig. 4) using the *WebPlotDigitizer* software. For the same set of experimental conditions (i.e. $Re = 474$, $T_{in} \approx 4.7^\circ\text{C}$, $T_{c,set} = -10^\circ\text{C}$), 5 independent measurements were performed.³ The results from the five measurements are highly consistent with each other, and a low uncertainty in the thickness of the ice layer was calculated of approximately $\sigma = 0.1 - 0.2$ mm based on the standard deviation from the mean. This uncertainty is assumed to be representative for the other experimental conditions as well, although it should be noted that in some measurements the true uncertainty might be larger due to uncertainties unaccounted for by the statistical analysis (such as a systematic uncertainty in determining $t = 0$ in the experiment). The obtained ice layer profiles agree well with the flow measurements and the raw camera images shown above (see Figs. 4 and 5). The maximum ice-thickness reached after 90 min is approximately 1.5 cm.

4.2. Ice growth for different cooling parameters and flow rates

Fig. 7 shows the growth of the ice layer at two different locations downstream in the channel, i.e. at $x = 5$ cm and $x = 75$ cm. The rate of ice growth decreases as the ice layer thickens, due to the combined effect of an increased thermal resistance of the ice and an enhanced heat transfer from the ‘warm’ fluid to the ice-water interface as the flow accelerates. This decrease in the ice growth rate is most pronounced near the inlet of the channel where the flow experiences significant development. A clear relationship is observed between the rate of ice growth and the

temperature of the cold plate: for a cold plate temperature of -10°C (corresponding to a cooling parameter of $\theta_c = \frac{T_m - T_c}{T_H - T_m} \approx 2$ for an inlet temperature of $T_{in} \approx 5^\circ\text{C}$) the ice after $t = 120$ min is almost twice as thick as for a cold plate temperature of -5°C . Likewise, a higher flow rate results in a decreased rate of ice growth, especially near the inlet of the channel where the heat-transfer from the fluid to the ice layer has a stronger dependence on the velocity. Near the inlet, for the smaller cooling parameters, a steady state ice layer thickness is reached. No steady state is reached within the centre of the channel for the given time-frame.

4.3. Evaluation of experimental boundary conditions

As mentioned earlier, one of the objectives of the design of the ESPRESSO facility was to have well-described experimental boundary conditions which can readily be implemented in numerical codes. Fig. 8 shows the temperature response of the cold plate for one of the freezing experiments where $Re = 474$, $T_{in} \approx 4.7^\circ\text{C}$, $T_{c,set} = -10^\circ\text{C}$. From these measurements, the boundary condition was derived which was imposed at the bottom of the cold plate in our numerical simulations.

The first three and a half hours correspond to the initial cooling of the water flow prior to the start of the experiment (as described in Section 2.3), indicated by the letter ‘A’. After approximately 30 min, when the temperature in the cold plate reaches 4°C , a sudden change in the temperature response is observed, indicated by the number ‘2’. Possibly, this is due to the onset of natural convection as a consequence of the anomalous expansion of water. After approximately 3 h and 45 min have passed, the flow-rate is lowered to the desired setpoint

³ For $t = 45$ min, no data is available for the third measurement.

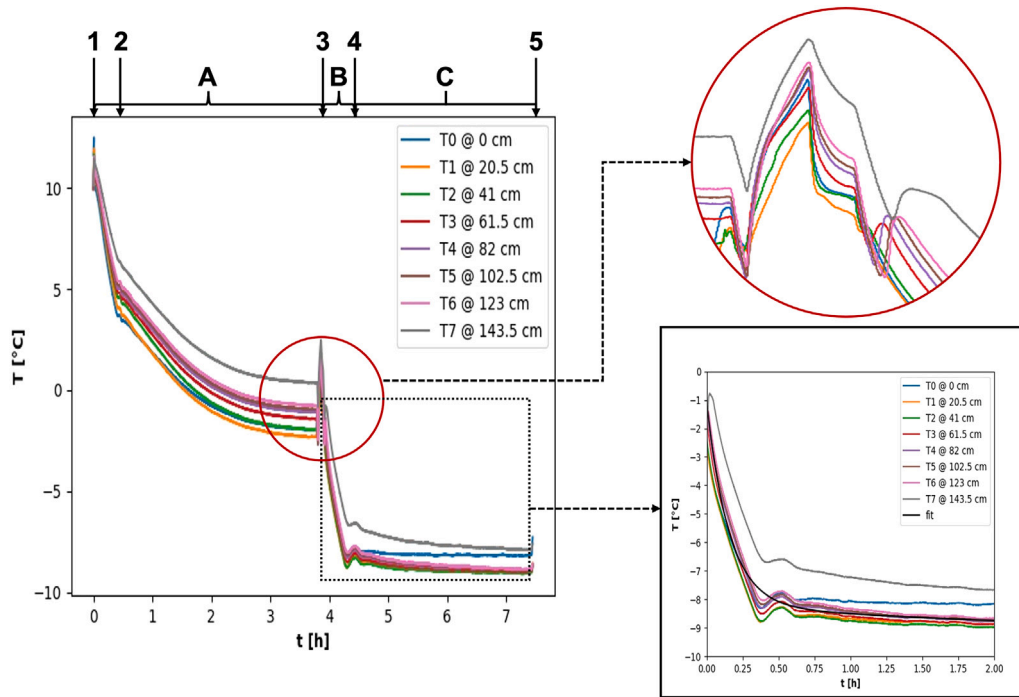


Fig. 8. Temperature response of the cold plate for all 8 thermo-couples, where the zoom-ins refer to the temperature response of the cold plate at the onset of ice-formation (where $t = 0$ is determined) and the transient temperature development after $t = 0$, including the empirical fit which can be used as a boundary condition in numerical simulations. The 3 different stages of the experiment are indicated by the letters A, B and C, where A refers to the initialization of the experiment prior to $t = 0$, B refers to roughly the first 30 min after $t = 0$ where the temperature in the cold plate experiences a significant transient and C refers to the remainder of the experiment at which a thermal equilibrium appears to exist between the coolant recirculating underneath the cold plate and the fluid flow in the square channel above. The numbers 1–5 refers to specific instances in the temperature evolution of the cold plate, 1 being the start of the experiment, 2 being a reduction in the rate at which the temperature declines, 3 being the onset of freezing, 4 being the establishment of thermal equilibrium within the cool-plate and 5 being the end of the experiments (where the pumps and the recirculating coolers are switched off). The experimental conditions were: $Re = 474$, $T_{in} \approx 4.7 \text{ }^\circ\text{C}$, $T_{c,set} = -10 \text{ }^\circ\text{C}$.

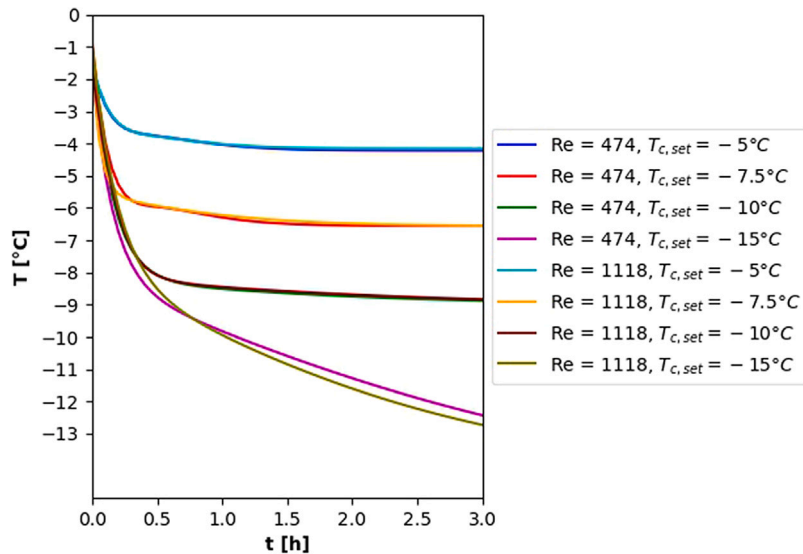


Fig. 9. Modelled transient behaviour of the cold plate for the 8 different experimental conditions, according to Eq. (21) and Table 2.

value. As described in Section 2.3, the test section is cleared of air bubbles by briefly increasing the flow rate to full capacity before the final reduction of the flow-rate to the setpoint value. The first temperature transient in the cold plate, indicated by the number ‘3’, corresponds to the rapid adjustment of the flow rate.

A second sudden change in the cold plate temperature (indicated by the number ‘4’), where the temperature increases from approximately $T_c = -2 \text{ }^\circ\text{C}$ to $T_c = -0.5 \text{ }^\circ\text{C}$ marks the onset of freezing, at which ice rapidly spreads over the entire plate. Such a sharp increase was also

observed by Savino et al. [26] and is possibly related to subcooling of the water prior to freezing, of which evidence had previously been provided by Savino et al. through a thermocouple measurement taken within the thermal boundary layer of the water during a short time span from before the ice was formed till after the probe became embedded within the ice-layer [26]. Based on the sequence of the thermo-couple response (with T0 being the first to respond and T7 the last), the nucleation of the ice is believed to commence at the inlet of the channel. The ice crystals rapidly propagate through the subcooled

Table 2

Model fit parameters of the transient cold plate response, as well as the averaged flow rates and inlet and outlet temperatures, for all 8 different experimental conditions.

	$T_{c,set}$	A	B	C	D	E	ϕ_c (L s ⁻¹)	T_{in} (°C)	T_{out} (°C)
Re = 474	-5 °C	10.071	3.373	7.429	2.251	-11.647	0.035 ± 0.004	4.46 ± 0.05	4.3 ± 0.1
	-7.5 °C	22.465	3.609	16.812	2.284	-23.369	0.035 ± 0.004	4.61 ± 0.09	4.3 ± 0.2
	-10 °C	7.040	6.363	0.791	-0.401	-8.215	0.034 ± 0.004	4.68 ± 0.05	4.1 ± 0.3
	-15 °C	6.410	6.303	6.631	-0.251	-8.205	0.035 ± 0.004	4.61 ± 0.08	4.2 ± 0.2
Re = 1118	-5 °C	9.220	3.509	6.602	2.292	-10.764	0.085 ± 0.004	4.56 ± 0.06	4.4 ± 0.1
	-7.5 °C	4.079	16.142	-1.000	0.781	-5.566	0.085 ± 0.004	4.45 ± 0.07	4.1 ± 0.3
	-10 °C	1.006	0.452	-6.329	4.139	-2.763	0.085 ± 0.004	4.8 ± 0.1	4.4 ± 0.4
	-15 °C	7.019	5.293	-6.282	0.328	-7.985	0.085 ± 0.004	4.59 ± 0.07	4.3 ± 0.2

water from the inlet to the outlet of the channel and the release of latent heat increases the temperature of the water. Since the water and the cold plate form a coupled system, a corresponding increase of the cold plate will follow as the cold plate adjusts to the new conditions, explaining the sudden sharp increase of the cold plate temperature.

During the first 30min following the onset of ice-formation, the temperatures in the cold plate continue to decrease until the setpoint value of the coolant is reached (indicated by the letter 'B'). Subsequently, a thermal equilibrium is established between the coolant recirculated underneath the test section and the water flowing through the test section. As a consequence, the temperature in the cold plate reaches a quasi steady state, at approximately 1 °C above the setpoint value of the coolant (indicated by the letter 'C'). The small decrease in the cold plate temperature still observed after the establishment of thermal equilibrium is probably a consequence of the growth of the ice layer, which acts as a thermal insulator.

Apart from entrance and exit effects (recognized by deviating temperature values for thermocouples T0 at the inlet and T7 at the exit of the cold plate), the differences between the temperatures of the other thermocouples (T1-T6) at a given time instance fall within the temperature uncertainty of the K-Type thermocouples (i.e. ±0.25 °C). For this reason, we suggest modelling the effect of the cold plate in the numerical simulations through a time-dependent, yet spatially uniform temperature boundary condition. In the present work, the following function is used as a reasonable approximation for the transient temperature behaviour of the cold plate:

$$A \exp(-Bt) + C \tanh(Dt) + E \quad (21)$$

The resulting fit parameters as well as the flow rate and inlet and outlet temperatures of the 8 different experimental conditions are shown in Table 2 and the fits are plotted in Fig. 9. A large degree of consistency was observed for both the flow rate and the bulk inlet temperature (which varied between approximately $T_{in} = 4.5\text{--}4.8$ °C)⁴. The bulk outlet temperature is slightly lower than the inlet temperature, as a consequence of the heat extracted by the cold plate. For practical purposes, the heat flux through the side and top walls of the test section was assumed to be negligible compared to the heat content of the recirculated water and the 1.7 kW capacity of the Julabo FL1701 cooler connected to the cold plate. For $T_{c,set} = -5$ °C and $T_{c,set} = -10$ °C, the first 30 min of the experiment were characterized by a significant transient as the cold plate approaches the set point value, after which a thermal equilibrium was established. However, for $T_{c,set} = -15$ °C the time required to achieve a thermal equilibrium exceeded the duration of the experiment. Some difference in the dynamics of the cold plate were observed between the two different flow rates, especially for the lowest set point temperature. However, it is unclear whether these differences were related to the flow rate or were caused by other factors (e.g. initialization procedure, ambient temperature, etc.).

⁴ In our simulations, a fit was also used for the inlet temperature (see Section 3.4).

4.4. Comparison with numerical results

Fig. 10 shows the results for the ice layer at the inlet and the absolute velocity profile at $x = 5$ cm obtained after the first 5 min, for three different mesh sizes. With respect to the reference mesh of approximately 380,000 elements, the other two meshes were coarsened 2 and 4 times in both the x and y directions, resulting in a mesh size of respectively 4 and 16 times smaller. The results for all three meshes for the velocity profile overlap and cannot be distinguished by eye. For the ice layer, the three meshes produce similar results although the finer meshes result in a smoother solution of the solid-liquid phase boundary. Therefore, the 380,000 mesh size was considered fully mesh convergent and was used throughout the rest of the transient simulations.

Fig. 11 shows the transient development of the ice layer obtained experimentally and numerically, for both the inlet and the centre of the channel. Near the inlet the thickness of the ice layer increases with the downstream distance. The spatial gradient in the ice layer becoming smaller as the distance to the inlet ($x = 0$) increases and near the centre of the channel the ice-profile appears to be (almost) flat, indicating the heat transfer is (close to) one-dimensional. A very good agreement with the experimental results was obtained, with the difference between the numerical results and experimental measurements on the sub-millimetre scale.

Fig. 12 shows the comparison between the experimental and numerical absolute velocity profiles, evaluated at $x = 5$ cm and $x = 75$ cm. A reasonable agreement between the experimental and numerical velocity profiles was obtained, however some discrepancies were observed. At $x = 5$ cm, the numerical velocity profiles have two local maxima, both left and right of the centre, whereas the experimentally measured velocity profiles only have one local maximum located around the centre of the domain. At $x = 75$ cm, the experimental and numerical velocity profiles display similar behaviour and a better agreement was observed between the experimental and numerical results as opposed to the results for $x = 5$ cm. Both follow a (near) parabolic velocity profile, with the velocity profile becoming more narrow as the ice layer thickens. However, the velocity values measured in the experiment were slightly higher than those obtained in the simulation. In addition, whereas the numerically calculated velocity profiles appear to be fully symmetric, the experimental velocity profiles appear to be slightly skewed towards the bottom wall of the test section, especially for the smaller ice thicknesses. Please note that the numerical simulations showed no evidence of (significant) buoyancy during the transient development of the ice-layer in the laminar channel flow, similar to the PIV measurements.

Possible explanations for the observed discrepancies are:

1. The numerical simulations were performed using a two-dimensional computational domain. The absence of the wall effect in the third dimension could lead to a different result for the numerical flow field than for the experimental flow-field. Indeed, it has been shown that the shape of the velocity profiles in rectangular channel deviates from classical Poiseuille flow. The stream-wise velocity profiles tend to be steeper near the walls

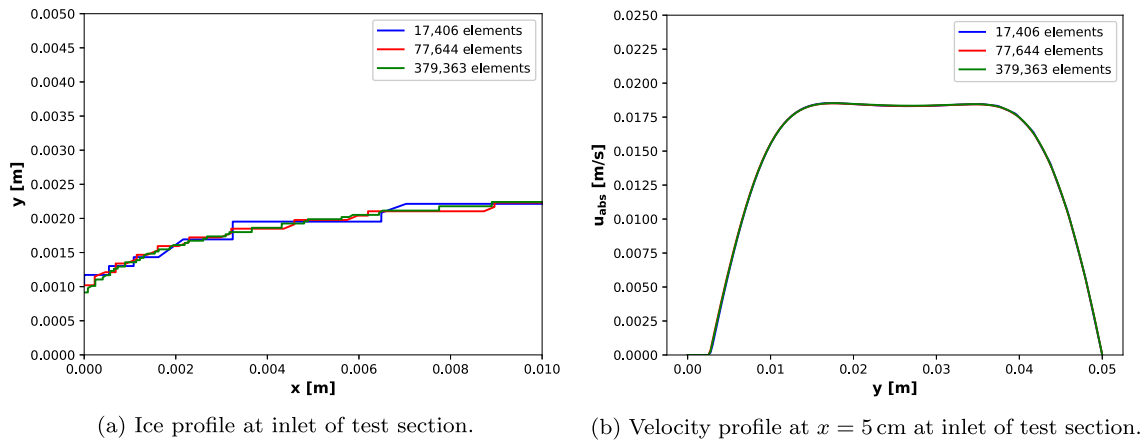


Fig. 10. Mesh refinement study for both the ice layer and the absolute velocity profile at the inlet. 3 meshes were considered, consisting of approximately 380,000, 77,644 and 17,406 elements respectively.

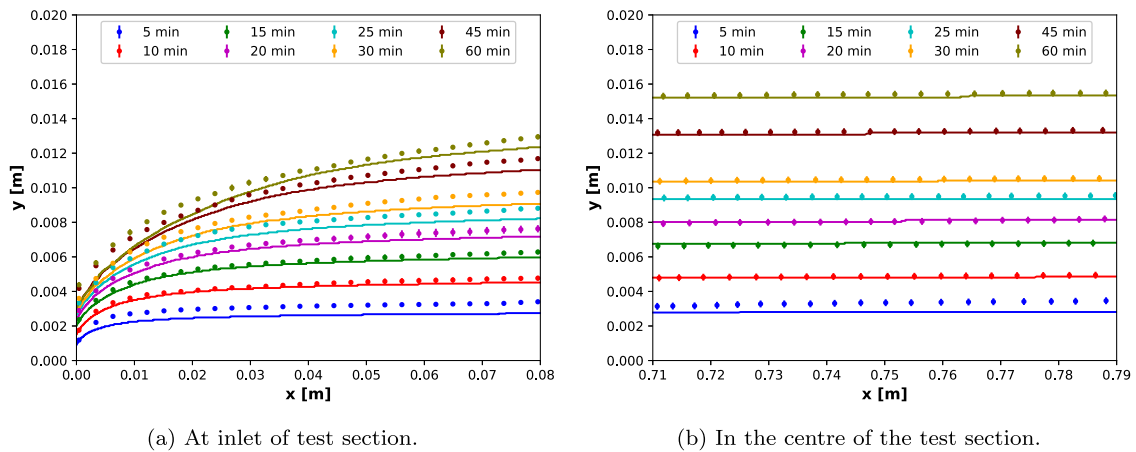


Fig. 11. Comparison between experimental and numerical ice profiles for different times after the onset of ice-formation. Two locations are shown, i.e. at the inlet of the test-section and at the centre. The experimental conditions were: $Re = 474$, $T_{in} \approx 4.7^\circ\text{C}$, $T_{c,set} = -10^\circ\text{C}$. The error bars for the experimental ice layer measurements at the inlet are given based on the statistical analysis of the five independent measurements performed for this case (see Fig. 6), the error bars for the experimental ice layer measurements at the centre of the channel are given based on the conservative error estimate of $\sigma = 0.2\text{ mm}$.

and flatter near the centre of the channel [48]. The transversal velocity components are largest near the entrance of the channel; for fully developed flow, the flow is approximately two-dimensional [49], explaining why a better agreement was obtained between the measured velocity profiles and our 2D simulations at the centre of the channel as compared to close to the inlet.

2. The assumptions used for the numerical simulation, including the use of the *Boussinesq* approximation for modelling buoyancy effects, the use of constant and isotropic thermophysical properties for the solid and liquid phases and the approximations of the inlet and boundary conditions. For the inlet conditions a uniform velocity profile was assumed, based on the predicted outlet condition of the contracting nozzle. However, the exact inlet conditions were not measured experimentally, since it was not possible to measure the velocity profile within the development length of $L = 13.5\text{cm}$ prior to the start of the test section.
3. Possible systematic errors when performing the experiments.

5. Conclusions and recommendations

This paper presents an experimental benchmark study on the transient freezing of water in a square channel under laminar flow conditions, where ice is grown from a cold plate at the bottom. This is one

of the few studies reporting the transient development of an ice layer in internal flow. In this work, both planar PIV velocity measurements and ice profiles sampled at multiple times during the experiment were presented, for both the inlet and the centre of the test-section. The measurement of the transient development of the ice-layer near the inlet of the channel is an important novelty of the present experimental campaign. Furthermore, a study was performed regarding the effect of the cooling parameter and the bulk velocity on the rate of the ice-growth. As such, a comprehensive and well-described experimental data set was generated for transient freezing in laminar internal flow to be used for numerical validation purposes.

The onset of ice-formation was found to coincide with a sudden increase of the cold-plate temperature. This behaviour of the cold plate was attributed to subcooling occurring in the thermal boundary layer prior to nucleation, based on the findings of *Savino et al.* [26]. The sequence of the thermocouples' response showed that ice nucleation first occurs at the inlet of the channel, from which the ice subsequently spreads over the entire cold plate surface. From the data provided by the thermocouples in the cold plate, we were able to define a set of boundary conditions which provided a simple yet accurate description of the conditions during the experimental campaign.

Water is characterized by an anomalous expansion behaviour during the freezing process, with a density inversion around 4°C . Based on the Richardson number, natural convection possibly played a role in our experiments. However, no evidence of (significant) natural convection

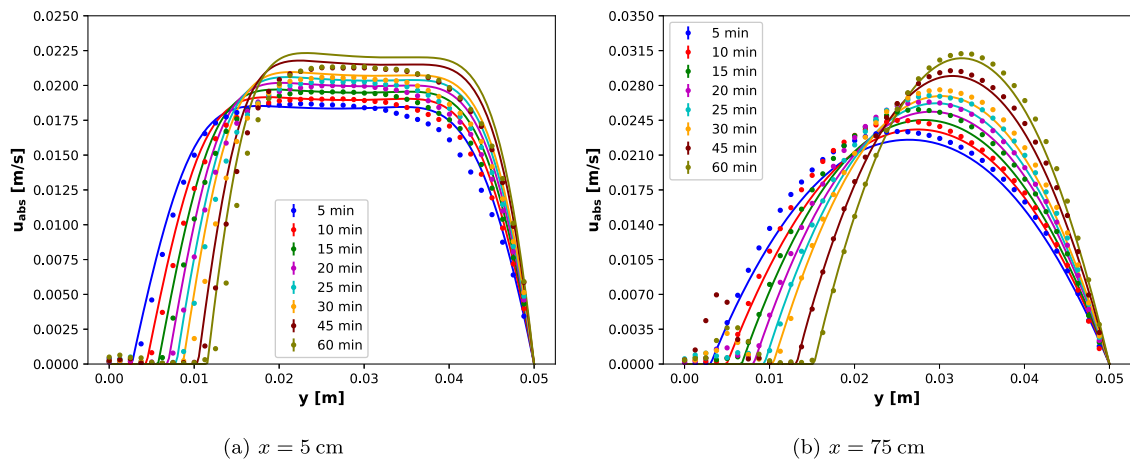


Fig. 12. Comparison between experimental and numerical velocity profiles evaluated at a distance of $x = 5$ cm and $x = 75$ cm from the inlet of the channel for different times after the onset of ice-formation. The experimental conditions were: $Re = 474$, $T_{in} \approx 4.7$ °C, $T_{c,set} = -10$ °C. Due to the small uncertainty on the experimental profiles, the error bars are not visible.

was present in our PIV flow measurements. Possibly, the constant motion of the fluid prevented the development of convection cells.

To demonstrate the suitability of the current experimental results for numerical validation purposes, a comparison with numerical simulations was included in this paper. The channel was approximated by a two-dimensional domain and included the cold-plate to account for conjugate heat transfer effects. Solid–liquid phase change was modelled through the linearized enthalpy approach, and the energy and momentum equations were discretized with the discontinuous Galerkin finite element method. The *Boussinesq* approximation was used to model natural convection, and the anomalous expansion of water was taken into account through a temperature-dependent thermal expansion coefficient. A very good agreement was obtained, both for the ice profiles and for the absolute velocity profiles, demonstrating the quality of the experimental results. Possible discrepancies were attributed to the use of a two-dimensional domain, the use of constant and isotropic thermo-physical properties within each phase and the use of an equal density for the water and the ice. Similar to the experiments, the numerical simulations showed no evidence of (significant) buoyancy during the transient development of the ice-layer in the laminar channel flow.

For future work, we recommend to perform stereoscopic PIV measurements to obtain the spanwise (z) velocity components, and to perform non-intrusive temperature measurements within the channel, for instance using laser induced fluorescence. Such measurements would be a further addition to the experimental benchmark data available for numerical model validation, in addition to providing insight into the possible generation of secondary flow during the transient development of the ice layer.

CRediT authorship contribution statement

Bouke Johannes Kaaks: Writing – original draft, Visualization, Validation, Software, Methodology, Investigation, Formal analysis, Data curation, Conceptualization. **Danny Lathouwers:** Writing – review & editing, Supervision, Funding acquisition, Conceptualization. **Jan-Leen Kloosterman:** Writing – review & editing, Supervision, Investigation. **Martin Rohde:** Writing – review & editing, Supervision, Methodology, Investigation, Funding acquisition, Conceptualization.

Declaration of competing interest

The authors declare that they have no known competing financial interests or personal relationships that could have appeared to influence the work reported in this paper.

Acknowledgements

We would like to thank our lab technicians Dick de Haas and John Vlieland, as well as Dimitri Kuznetsov, Pieter van den Oever and Reinier den Oudsten from DEMO, for their help in designing and building the ESPRESSO experimental facility.

This project has received funding from the H2020 Euratom research and training programme 2014–2018 under grant agreement no. 847527. A preprint of this paper is available at [doi:10.2139/ssrn.4360285](https://doi.org/10.2139/ssrn.4360285).

Data availability

The experimental data from the PIV measurements is made available at <https://doi.org/10.5281/zenodo.7573327> and the data from the numerical simulations can be found at <https://doi.org/10.5281/zenodo.7602394>.

References

- [1] C. Gau, R. Viskanta, Melting and solidification of a pure metal on a vertical wall, *J. Heat Transfer* 108 (1986) 174–181.
- [2] T.A. Campbell, J.N. Koster, Visualization of liquid-solid interface morphologies in gallium subject to natural convection, *J. Cryst. Growth* (ISSN: 00220248) 140 (3–4) (1994) 414–425.
- [3] O. Ben-David, A. Levy, B. Mikhailovich, A. Azulay, 3D numerical and experimental study of gallium melting in a rectangular container, *Int. J. Heat Mass Transfer* (ISSN: 0017-9310) 67 (2013) 260–271, <http://dx.doi.org/10.1016/j.ijheatmasstransfer.2013.07.058>.
- [4] J. Vogel, D. Bauer, Phase state and velocity measurements with high temporal and spatial resolution during melting of *n*-octadecane in a rectangular enclosure with two heated vertical sides, *Int. J. Heat Mass Transfer* (ISSN: 0017-9310) 127 (2018) 1264–1276, <http://dx.doi.org/10.1016/j.ijheatmasstransfer.2018.06.084>.
- [5] M. Faden, C. Linhardt, S. Höhle, A. König-Haagen, D. Brüggemann, Velocity field and phase boundary measurements during melting of *n*-octadecane in a cubical test cell, *Int. J. Heat Mass Transfer* (ISSN: 00179310) 135 (2019) 104–114, <http://dx.doi.org/10.1016/j.ijheatmasstransfer.2019.01.056>.
- [6] M. Tiberge, D. Shafer, D. Lathouwers, M. Rohde, J.L. Kloosterman, Preliminary investigation on the melting behavior of a freeze-valve for the molten salt fast reactor, *Ann. Nucl. Energy* (ISSN: 18732100) 132 (2019) 544–554, <http://dx.doi.org/10.1016/j.anucene.2019.06.039>.
- [7] G. Cartland Glover, A. Skillen, D. Litskevich, S. Rolfo, D.R. Emerson, B. Merk, C. Moulinec, On the numerical modelling of frozen walls in a molten salt fast reactor, *Nucl. Eng. Des.* (ISSN: 00295493) 355 (March) (2019) 110290, <http://dx.doi.org/10.1016/j.nucengdes.2019.110290>.
- [8] N. Le Brun, G.F. Hewitt, C.N. Markides, Transient freezing of molten salts in pipe-flow systems: Application to the direct reactor auxiliary cooling system (DRACS), *Appl. Energy* (ISSN: 03062619) 186 (2017) 56–67, <http://dx.doi.org/10.1016/j.apenergy.2016.09.099>.

- [9] V. Voulgaropoulos, N.L. Brun, A. Charogiannis, C.N. Markides, Transient freezing of water between two parallel plates: A combined experimental and modelling study, *Int. J. Heat Mass Transfer* (ISSN: 00179310) 153 (2020) 119596, <http://dx.doi.org/10.1016/j.ijheatmasstransfer.2020.119596>.
- [10] T.A. Kowalewski, M. Rebow, Freezing of water in a differentially heated cubic cavity, *Int. J. Comput. Fluid Dyn.* (ISSN: 10618562) 11 (3–4) (1999) 193–210.
- [11] R.D. Zerkle, J.E. Sunderland, The effect of liquid solidification in a tube upon laminar-flow heat transfer and pressure drop, *J. Heat Transfer* (ISSN: 15288943) 90 (2) (1968) 183–189.
- [12] A.P. Arora, J.R. Howell, An investigation of the freezing of supercooled liquid in forced turbulent flow inside circular tubes, *Int. J. Heat Mass Transfer* (ISSN: 00179310) 16 (11) (1973) 2077–2085.
- [13] J.C. Mulligan, D.D. Jones, Experiments on heat transfer and pressure drop in a horizontal tube with internal solidification, *Int. J. Heat Mass Transfer* (ISSN: 00179310) 19 (2) (1976) 213–219.
- [14] T. Hirata, R.R. Gilpin, K.C. Cheng, E.M. Gates, The steady state ice layer profile on a constant temperature plate in a forced convection flow- I. Laminar regime, *Int. Commun. Heat Mass Transfer* 22 (1979) 1425–1433.
- [15] Y. Kikuchi, Y. Shigemasa, T. Ogata, Steady-state freezing of liquids in laminar flow between two parallel plates, *J. Nucl. Sci. Technol.* (ISSN: 00223131) 23 (11) (1986) 979–991.
- [16] M.C. Holmes-Cerfon, J.A. Whitehead, Instability and freezing in a solidifying melt conduit, *Physica D* (ISSN: 01672789) 240 (2) (2011) 131–139, <http://dx.doi.org/10.1016/j.physd.2010.10.009>.
- [17] T. Hirata, R.R. Gilpin, K.C. Cheng, The steady state ice layer profile on a constant temperature plate in a forced convection flow-II. The transition and turbulent regimes, *Int. J. Heat Mass Transfer* (ISSN: 00179310) 22 (10) (1979) 1435–1443.
- [18] R.R. Gilpin, T. Hirata, K.C. Cheng, Wave formation and heat transfer at an ice-water interface in the presence of a turbulent flow, *J. Fluid Mech.* (ISSN: 14697645) 99 (3) (1980) 619–640.
- [19] N. Seki, S. Fukusako, G.W. Younan, Ice-formation phenomena for water flow between two cooled parallel plates, *J. Heat Transfer* (ISSN: 15288943) 106 (3) (1984) 498–505.
- [20] T. Hirata, H. Matsuzawa, Study of ice shape on freezing of flowing water in a pipe, *Trans. Jpn. Soc. Mech. Eng. Ser. B* (ISSN: 03875016) 53 (486) (1987) 553–559.
- [21] B. Weigand, H. Beer, Solidification of flowing liquid in an asymmetric cooled parallel-plate channel, *Int. Commun. Heat Mass Transfer* (ISSN: 07351933) 19 (1) (1992) 17–27, [http://dx.doi.org/10.1016/0735-1933\(92\)90060-U](http://dx.doi.org/10.1016/0735-1933(92)90060-U).
- [22] M. Tago, S. Fukusako, M. Yamada, A. Horibe, An experimental study of ice-layer transition phenomena in a rectangular duct containing water flow, *Wärme-Stoffübertragung* (ISSN: 00429929) 28 (1–2) (1993) 37–47.
- [23] T. Hirata, M. Ishihara, Freeze-off conditions of a pipe containing a flow of water, *Int. J. Heat Mass Transfer* (ISSN: 00179310) 28 (2) (1985) 331–337.
- [24] M.N. Özişik, J.C. Mulligan, Transient freezing of liquids in forced flow inside circular tubes, *J. Heat Transfer* (ISSN: 15288943) 91 (3) (1969) 385–389.
- [25] B. Weigand, H. Beer, Transient freezing of liquids in forced laminar flow inside a parallel plate channel, *Wärme- Stoffübertragung* (ISSN: 00429929) 27 (2) (1992) 77–84.
- [26] J.M. Savino, Experimental and Analytical Study of the Transient Solidification of a Warm Liquid Flowing Over a Chilled Flat Plate, *Tech. Rep.*, National Aeronautics and Space Administration, 1967.
- [27] E. Ramudu, B.H. Hirsh, P. Olson, A. Gnanadesikan, Turbulent heat exchange between water and ice at an evolving ice-water interface, *J. Fluid Mech.* (ISSN: 14697645) 798 (2016) 572–597.
- [28] M. Bushuk, M. Bushuk, D.M. Holland, T.P. Stanton, A. Stern, C. Gray, Ice scallops: a laboratory investigation of the ice-water interface, *J. Fluid Mech.* (ISSN: 14697645) 873 (2019) 942–976.
- [29] J.W. C.O. Popiel, Thermophysical properties, *Heat Transf. Eng.* 19 (3) (1998) 87–101.
- [30] O. Benes, M. Salanne, M. Levesque, R. Konings, Physico-Chemical Properties of the MSFR Fuel Salt Evaluation and Viability of Liquid Fuel Fast Reactor System, *Tech. Rep.*, 2013.
- [31] E. Large, C.D. Andereck, Penetrative Rayleigh-Bénard convection in water near its maximum density point, *Phys. Fluids* (ISSN: 10897666) 26 (9) (2014) <http://dx.doi.org/10.1063/1.4895063>.
- [32] V. Kumar, M. Kumawat, A. Srivastava, S. Karagadde, Mechanism of flow reversal during solidification of an anomalous liquid, *Phys. Fluids* (ISSN: 10897666) 29 (12) (2017) <http://dx.doi.org/10.1063/1.5005139>.
- [33] R.M. Manglik, A.E. Bergles, Heat transfer and pressure drop correlations for the rectangular offset strip fin compact heat exchanger, *Exp. Therm Fluid Sci.* (ISSN: 08941777) 10 (2) (1995) 171–180.
- [34] R.D. Mehta, P. Bradshaw, Technical notes of design for small low speed wind tunnels, *Aeronaut. J. R. Aeronaut. Soc.* (ISSN: 0001-9240) (7) (1979) 1, 445, 446 & 448.
- [35] J. Scheiman, Comparison of experimental and theoretical turbulence reduction characteristics for screens, honeycomb, and honeycomb-screen combinations, *NASA Tech. Pap.* (ISSN: 01488341) (December 1981) (1981).
- [36] J.H. Bell, R.D. Mehta, for Small Low-Speed Wind Tunnels, *Tech. Rep.* August, 1988, pp. 1–39.
- [37] R.J. Adrian, J. Westerweel, *Particle Image Velocimetry*, First ed., Cambridge University Press, ISBN: 978-0-521-44008-0, 2011.
- [38] B.J. Kaaks, M. Rohde, J.-I. Kloosterman, D. Lathouwers, An energy-conservative DG-FEM approach for solid-liquid phase change, *Numer. Heat Transfer B* (ISSN: 1040-7790) (2023) 1–27, URL <https://www.tandfonline.com/doi/full/10.1080/10407790.2023.2211231>.
- [39] A.D. Brent, V.R. Voller, K.J. Reid, Enthalpy-porosity technique for modeling convection-diffusion phase change: Application to the melting of a pure metal, *Numer. Heat Transfer* (ISSN: 01495720) 13 (3) (1988) 297–318.
- [40] C. Bonacina, G. Comini, A. Fasano, M. Primicerio, Numerical solution of phase-change problems, *Int. J. Heat Mass Transfer* (ISSN: 00179310) 16 (10) (1973) 1825–1832.
- [41] M. Tiberger, D. Lathouwers, J.L. Kloosterman, A multi-physics solver for liquid-fueled fast systems based on the discontinuous Galerkin FEM discretization, *Prog. Nucl. Energy* (ISSN: 01491970) 127 (May) (2020) 103427, URL <https://doi.org/10.1016/j.pnucene.2020.103427>.
- [42] A. Hennink, M. Tiberger, D. Lathouwers, A pressure-based solver for low-mach number flow using a discontinuous Galerkin method, *J. Comput. Phys.* (ISSN: 10902716) 425 (2021) 109877, <http://dx.doi.org/10.1016/j.jcp.2020.109877>.
- [43] B. Nedjar, An enthalpy-based finite element method for nonlinear heat problems involving phase change, *Comput. Struct.* (ISSN: 00457949) 80 (1) (2002) 9–21.
- [44] M. Faden, A. König-Haagen, E. Franquet, D. Brüggemann, Influence of density change during melting inside a cavity: Theoretical scaling laws and numerical analysis, *Int. J. Heat Mass Transfer* (ISSN: 00179310) 173 (2021).
- [45] Y. Belhamadia, A.S. Kane, A. Fortin, An enhanced mathematical model for phase change problems with natural convection, *Int. J. Numer. Anal. Model. Ser. B* 3 (2) (2012) 192–206.
- [46] A. König-Haagen, E. Franquet, M. Faden, D. Brüggemann, Influence of the convective energy formulation for melting problems with enthalpy methods, *Int. J. Therm. Sci.* (ISSN: 12900729) 158 (July) (2020).
- [47] C. Kuan-Cheng, J. Ouazzani, F. Rosenberger, Mixed convection between horizontal plates-II. Fully developed flow, *Int. J. Heat Mass Transfer* (ISSN: 00179310) 30 (8) (1987) 1655–1662.
- [48] A.S. Berman, Laminar flow in channels with porous walls, *J. Appl. Phys.* (ISSN: 00218979) 24 (9) (1953) 1232–1235.
- [49] G. Hwang, Y. Cheng, Developing laminar flow and heat transfer in a square duct with one-walled injection and suction, *Int. J. Heat Mass Transfer* 36 (9) (1993) 2429–2440.